

Classes of hydrodynamic and magnetohydrodynamic turbulent decay

Axel Brandenburg^{1,2,3,4,*} and Tina Kahniashvili^{5,6,7,†}

¹Laboratory for Atmospheric and Space Physics, University of Colorado, Boulder, CO 80303, USA

²JILA and Department of Astrophysical and Planetary Sciences,
University of Colorado, Boulder, CO 80303, USA

³Nordita, KTH Royal Institute of Technology and Stockholm University, Roslagstullsbacken 23, 10691 Stockholm, Sweden

⁴Department of Astronomy, AlbaNova University Center, Stockholm University, 10691 Stockholm, Sweden

⁵The McWilliams Center for Cosmology and Department of Physics,
Carnegie Mellon University, 5000 Forbes Ave, Pittsburgh, PA 15213, USA

⁶Department of Physics, Laurentian University, Ramsey Lake Road, Sudbury, ON P3E 2C, Canada

⁷Abastumani Astrophysical Observatory, Iliia State University,
3-5 Cholokashvili Ave, Tbilisi, GE-0194, Georgia

(Dated: Received 5 July 2016; published 3 February 2017, Revision: 1.66)

We perform numerical simulations of decaying hydrodynamic and magnetohydrodynamic turbulence. We classify our time-dependent solutions by their evolutionary tracks in parametric plots between instantaneous scaling exponents. We find distinct classes of solutions evolving along specific trajectories toward points on a line of self-similar solutions. These trajectories are determined by the underlying physics governing individual cases, while the infrared slope of the initial conditions plays only a limited role. In the helical case, even for a scale-invariant initial spectrum (inversely proportional to wavenumber k), the solution evolves along the same trajectory as for a Batchelor spectrum (proportional to k^4).

PACS numbers: 98.70.Vc, 98.80.-k

The study of *decaying* turbulence is as old as that of turbulence itself. Being independent of an ill-defined forcing mechanism, decaying turbulence has a better chance in displaying generic properties of turbulence. Such properties are usually reflected in the existence of conserved quantities such as the Loitsiansky integral [1] and the magnetic helicity [2, 3]. Important applications of decaying turbulence include grid turbulence [4], turbulent wakes [5], atmospheric turbulence [6], as well as interstellar turbulence [7], galaxy clusters [8], and the early Universe [9, 10]. In the latter case, cosmological magnetic fields generated in the early Universe provide the initial source of turbulence, which leads to a growth of the correlation length by an inverse cascade mechanism [11], in addition to the general cosmological expansion of the Universe. In the last two decades, this topic has gained significant attention [12]. The time span since the initial magnetic field generation is enormous, but it is still uncertain whether it is long enough to produce fields at sufficiently large length scales to explain the possibility of contemporary magnetic fields in the space between clusters of galaxies [13].

In this Letter, we use direct numerical simulations (DNS) of both hydrodynamic (HD) and magnetohydrodynamic (MHD) decaying turbulence to classify different types by their decay behavior. The decay is characterized by the temporal change of the kinetic energy spec-

trum, $E_K(k, t)$, and, in MHD, also by the magnetic energy spectrum, $E_M(k, t)$. Here, k is the wavenumber and t is time. In addition to the decay laws of the energies $\mathcal{E}_i(t) = \int E_i(k, t) dk$, with $i = K$ or M for kinetic and magnetic energies, there are the kinetic and magnetic integral scales,

$$\xi_i(t) = \int_0^\infty k^{-1} E_i(k, t) dk / \int_0^\infty E_i(k, t) dk. \quad (1)$$

We quantify the decay by the instantaneous scaling exponents $p(t) \equiv d \ln \mathcal{E} / d \ln t$ and $q(t) \equiv d \ln \xi / d \ln t$. Thus, we study the decay behaviors by plotting $p(t)$ vs. $q(t)$ in a parametric representation. The pq diagram turns out to be a powerful diagnostic tool.

Earlier work [8, 14, 15] has suggested that the decay behavior, and thus the positions of solutions in the pq diagram, depend on the exponent α for initial conditions of the form $E \sim k^\alpha e^{-k/k_0}$, where k_0 is a cutoff wavenumber. Motivated by earlier findings [2, 11] of an inverse cascade in decaying MHD turbulence, Olesen considered the time-dependent energy spectra $E(k, t)$ to be of the form [15]

$$E(k, t) \propto k^\alpha \psi(k\xi(t)), \quad (2)$$

where $\xi(t) \propto t^q$, with q being an as yet undetermined scaling exponent, and ψ is a function that depends on the dissipative and turbulent processes that lead to a departure from a powerlaw at large k . Moreover, the slope $\psi' \equiv d\psi/d\kappa$ with $\kappa = k\xi$ must vanish for $\kappa \rightarrow 0$. This turns out to be a critical restriction.

Olesen then makes use of the fact that the HD and MHD equations are invariant under rescaling, $x \rightarrow \tilde{x}\ell$

*Electronic address: brandenb@nordita.org

†Electronic address: tinatin@andrew.cmu.edu

and $t \rightarrow \tilde{t}\ell^{1/q}$, which implies corresponding rescalings for velocity $u \rightarrow \tilde{t}\ell^{1-1/q}$ and viscosity $\nu \rightarrow \tilde{\nu}\ell^{2-1/q}$. Furthermore, using the fact that the dimensions of $E(k, t)$ are given by $[E] = [x]^3[t]^{-2}$, and requiring ψ to be invariant under rescaling $E \rightarrow \tilde{E}\ell^{3-2/q} \propto \tilde{k}^\alpha \ell^{-\alpha} \psi$, he finds from Eq. (2) that $\alpha = -3 + 2/q$. He argues that for a given subinertial range spectral exponent α , the exponent q is given by [12, 15–17]

$$q = 2/(3 + \alpha) \quad (3)$$

for both HD and MHD and independent of the presence or absence of helicity. A remarkable prediction of Olesen’s original work concerns the existence of inverse transfer even in the absence of magnetic helicity, provided $\alpha > -3$. In subsequent work he stresses that for constant ν (and η), only the case $\alpha = 1$ can be realized. For nonhelical MHD, this is indeed compatible with simulations [23–25], but not for HD [26] nor for helical MHD [3, 18].

In this Letter, we argue that the scaling exponent q is *not* primarily determined by the initial value of α , as suggested by Eq. (3), but by the physical processes involved. Moreover, we relax the restriction $\psi'(0) = 0$ and write instead

$$E(k\xi(t), t) = \xi^{-\beta} \phi(k\xi), \quad (4)$$

where $\xi = \xi(t)$ is computed from Eq. (1), and β needs to be determined empirically or theoretically. Clearly, the initial powerlaw slope at small k is no longer an adjustable input parameter, but is fixed by the form of $\phi = \phi(\kappa)$. Specifically, the “intrinsic” slope is $\alpha_* \equiv d \ln \phi / d \ln \kappa$. Evidently, ψ can be computed from ϕ as $\psi(\kappa) = \xi^{\alpha-\beta} \phi(\kappa) / \kappa^\alpha$, but, in general, $d \ln \psi / d \ln \kappa = \alpha_* - \alpha \neq 0$ for $\kappa \rightarrow 0$.

In the following, we study examples of different decay behaviors in the diagnostic pq diagram using data from DNS. As in earlier work [18], we solve the nonideal HD and MHD equations for an isothermal equation of state, i.e., pressure P and density ρ are proportional to each other, $P = \rho c_s^2$, where $c_s = \text{const}$ is the sound speed. The kinematic viscosity ν is characterized by the Reynolds number, $\text{Re} = u_{\text{rms}} \xi / \nu$, with $u_{\text{rms}} = (2\mathcal{E})^{1/2}$ and the magnetic diffusivity η is characterized by the magnetic Prandtl number $\text{Pr}_M = \nu / \eta$. The governing equations are solved using the PENCIL CODE [19, 20]. The resolution is either 1152^3 or 2304^3 meshpoints. The Mach number u_{rms} / c_s is always below unity, so compressibility effects are weak.

We first consider cases that have $\alpha = 4$ for the initial spectral slopes of E_K or E_M . We consider (i) HD decay, (ii) nonhelical MHD decay, and (iii) helical MHD decay. In cases (ii) and (iii), the magnetic energy also drives kinetic energy through the Lorentz force. The particular simulation of case (ii) was already presented in Ref. [23], where inverse transfer to smaller wavenumbers was found

in the absence of magnetic helicity using high-resolution DNS. Case (iii) leads to standard inverse transfer [2, 3, 9, 10]. The resulting spectra are plotted in Figs. 1(a)–(c), where we show energy spectra for cases (i)–(iii) at different times. The values of Re at half time are roughly 100, 230, and 300, respectively.

In Figs. 1(d)–(f) we compare with suitably compensated spectra. We compensate for the shift in k by plotting $E(k, t)$ against $k\xi(t)$. The peak in each spectrum, which is approximately at $k = \xi^{-1}$, has then always the same position on the abscissa. Furthermore, to compensate for the decay in energy, we multiply E by ξ^β with some exponent β such that the compensated spectra collapse onto a single function $\phi(k\xi(t)) \approx \xi^\beta E(k\xi(t), t)$. In terms of the energy $\mathcal{E}(t) \equiv \int E(k, t) dk$, the function $\Phi = \xi^{\beta+1} \mathcal{E}_K$ is asymptotically constant, $\Phi(t) \rightarrow \Phi_\infty$, and has the same dimension as ϕ , so we plot the nondimensional ratio ϕ / Φ_∞ . The function $\psi(\kappa)$ is shown as an inset and normalized by $\Psi_* \equiv \xi^{\alpha-\beta} \Phi$ at the last time.

Let us now consider solutions (i)–(iii) in the pq diagram; see Figs. 2(a)–(c). These are compatible with independently computed βq diagrams [20]. To study the relation between the exponents β and q , we make use of Olesen’s scaling arguments and that ϕ is invariant under rescaling, to show from Eq. (4) that $\beta + 3 - 2/q = 0$, i.e.,

$$\beta = 2/q - 3, \quad (5)$$

or $q = 2/(3 + \beta)$. This is formally equivalent to Olesen’s relation (3), but with α being replaced by β . Moreover, unlike the exponent α in Eq. (2), the exponent β in Eq. (4) bears no relation with the initial spectral slope, except for certain cases discussed below. The temporal decay of kinetic and magnetic energies follows power laws $\mathcal{E}_i(t) \sim t^{-p_i}$ for $i = K$ or M . The exponents are obtained by integrating over k , $\mathcal{E}(t) = \xi^{-(\beta+1)} \int \phi d(k\xi) \propto t^{-p}$, and since $\xi \propto t^q$, this yields

$$p = (1 + \beta)q. \quad (6)$$

Thus, in a pq diagram, a certain value of β corresponds to a line $p(t) \propto q(t)$ with the slope $\beta + 1$. Furthermore, inserting Eq. (5) yields the line $p = 2(1 - q)$. We call this the self-similarity line.

The exponents β , p , and q are roughly consistent with those expected based on the dimensions of potentially conserved quantities such as the Loitsiansky integral [28], $\mathcal{L} = \int \mathbf{r}^2 \langle \mathbf{u}(\mathbf{x}) \cdot \mathbf{u}(\mathbf{x} + \mathbf{r}) \rangle d\mathbf{r} \propto \ell^5 u_\ell^2$, with typical velocity u_ℓ on scale ℓ , the magnetic helicity, $\langle \mathbf{A} \cdot \mathbf{B} \rangle$, where $\mathbf{B} = \nabla \times \mathbf{A}$ is the magnetic field in terms of the vector potential \mathbf{A} , and the mean squared vector potential, $\langle \mathbf{A}^2 \rangle$, which is conserved in two-dimensions (2D); see Table I.

In the HD case (i), the solution approaches the $\beta = 3$ line and then settles on the self-similarity line at $q \approx 1/3$; see Fig. 2(a). This decay behavior departs from what would be expected if the Loitsiansky integral were conserved, i.e., $q = 2/7$ and $\beta = 4$. A slower decay

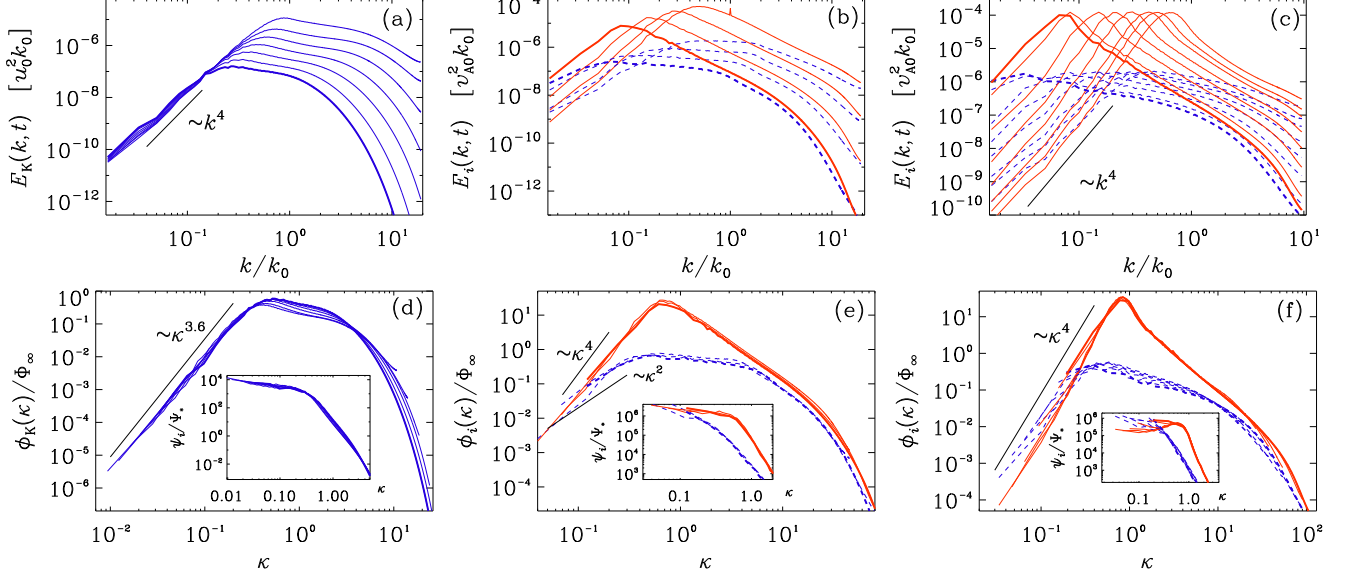


FIG. 1: $E_K(k, t)$ for different t in HD DNS (a), compared with E_M (solid red) and E_K (dashed blue) in MHD without helicity (b), and with (c). Panels (d)–(f) show collapsed spectra using $\beta = 3$ (d), $\beta = 1$ (e), and $\beta = 0$ (f).

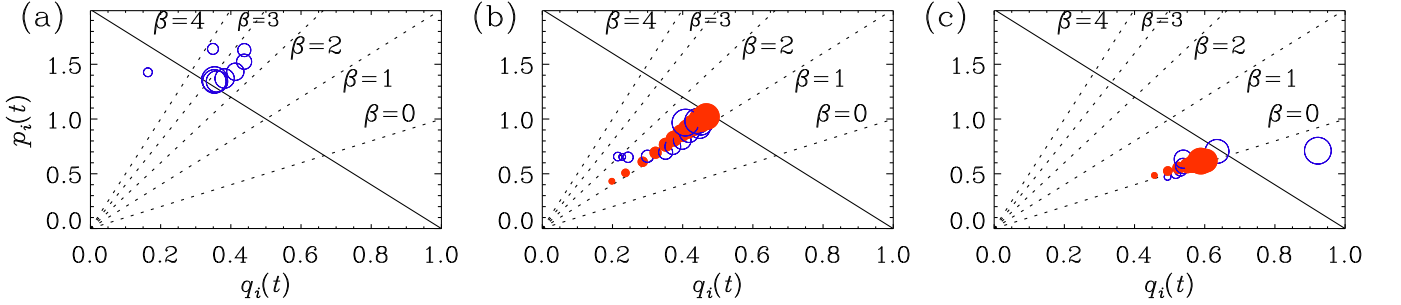


FIG. 2: pq diagrams for cases (i)–(iii). Open (closed) symbols correspond to $i = K$ (M) and their sizes increase with time.

law with $p = 6/5$, corresponding to $q = 2/5$ and $\beta = 2$ has been favored by Saffman [29], while experiments and simulations suggest $p = 5/4$ [26, 30].

In case (ii), the solution evolves along $\beta = 1$ toward $q = 1/2$; see Figs. 2(b) and (e). This is compatible with the conservation of $\langle \mathbf{A}_{2D}^2 \rangle$, where \mathbf{A}_{2D} is the component of \mathbf{A} which describes the 2D magnetic field in the plane

perpendicular to the local intermediate eigenvector of the rate-of-strain matrix \mathbf{S} ; see the supplemental material of [23] for details, and also [31]. The motivation for applying 2D arguments to 3D comes from the fact that for sufficiently strong magnetic fields the dynamics tends to become locally 2D in the plane perpendicular to the local field. This allows one to compute \mathbf{A} in a gauge that projects out contributions perpendicular to the intermediate eigenvector of \mathbf{S} .

In case (iii) the solution evolves along $\beta = 0$ toward $q = 2/3$; see Figs. 2(c) and (f). This means that the spectrum shifts just in k , while the amplitude of E_M does not change, as can be seen from Fig. 1(c). This is consistent with the invariance of $\langle \mathbf{A} \cdot \mathbf{B} \rangle$; see Ref. [3].

Next, we investigate cases with $\alpha < 4$. In the helical case with $\alpha = 2$ we see that the subinertial range spectrum quickly steepens and approaches $\alpha_* = 4 \neq \alpha$; see Figs. 3(a)–(c). For $\alpha = -1$, which is a scale-invariant spectrum, the spectral energy remains nearly unchanged at small k , but the magnetic energy still decays due to

TABLE I: Scaling exponents and relation to physical invariants and their dimensions.

β	p	q	inv.	dim.
4	$10/7 \approx 1.43$	$2/7 \approx 0.286$	\mathcal{L}	$[x]^7 [t]^{-2}$
3	$8/6 \approx 1.33$	$2/6 \approx 0.333$		
2	$6/5 = 1.20$	$2/5 = 0.400$		
1	$4/4 = 1.00$	$2/4 = 0.500$	$\langle \mathbf{A}_{2D}^2 \rangle$	$[x]^4 [t]^{-2}$
0	$2/3 \approx 0.67$	$2/3 \approx 0.667$	$\langle \mathbf{A} \cdot \mathbf{B} \rangle$	$[x]^3 [t]^{-2}$
-1	$0/2 = 0.00$	$2/1 = 1.000$		

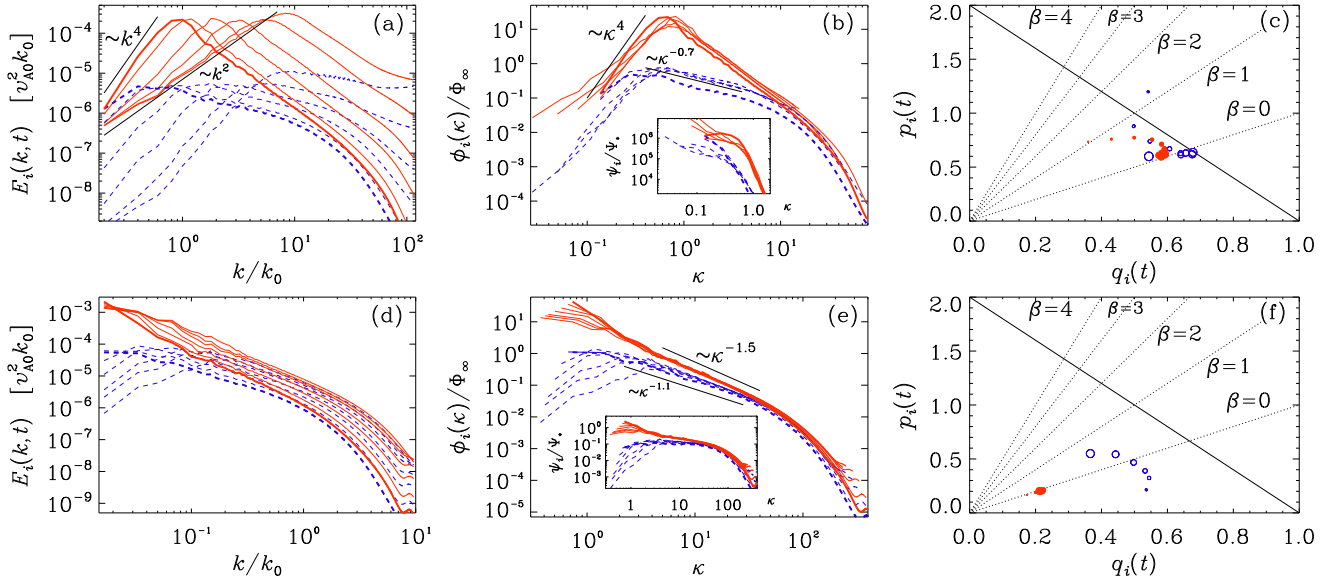


FIG. 3: E_M (solid) and E_K (dashed) in MHD with fractional helicity and $\alpha = 2$ (a), as well as full helicity and $\alpha = -1$ (d), together with compensated spectra (b,e) and the pq diagrams (c,f).

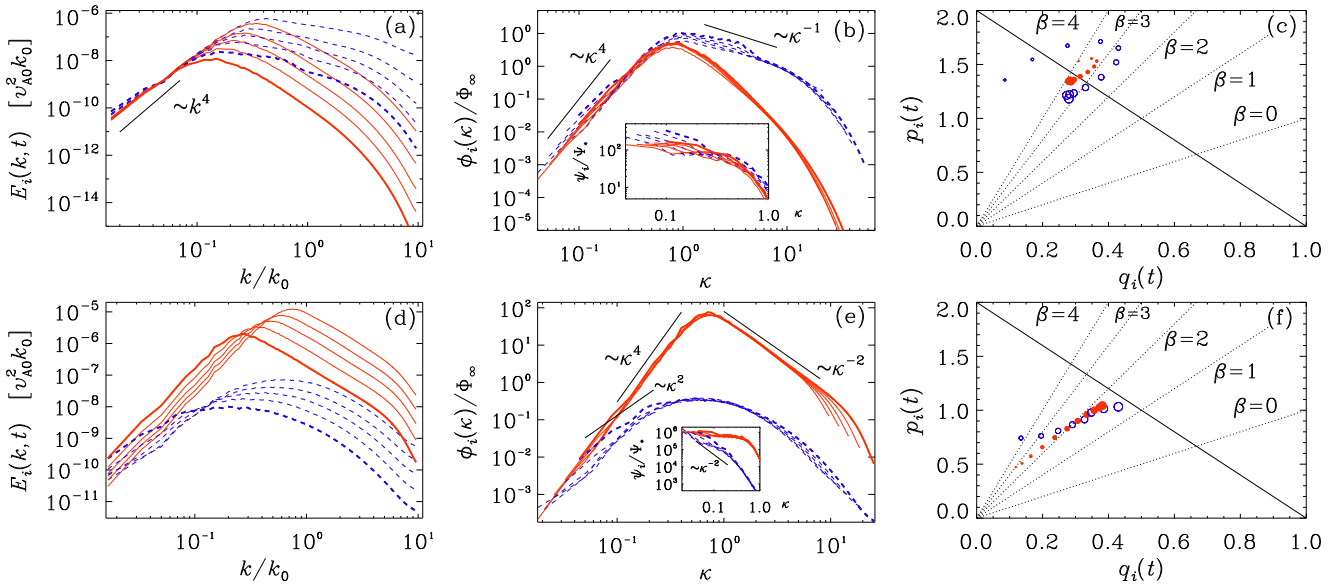


FIG. 4: Similar to Fig. 3, but for nonhelical MHD with $\text{Pr}_M = 0.01$ (a) and $\text{Pr}_M = 100$ (d), together with compensated spectra (b,e) and the pq diagrams (c,f).

decay at all higher k ; see Figs. 3(d)–(f). The values of p_M and q_M are rather small (≈ 0.2), but the spectra can still be collapsed onto each other with $\beta = 0$; see Fig. 3(e).

The examples discussed above demonstrate that in general $\beta \neq \alpha \neq \alpha_*$, i.e., the self-similarity parameter β is not determined by the initial power spectrum but rather by the different physical processes involved. In helical MHD, we always find $\alpha_* = 4$ together with $\beta = 0$. For nonhelical MHD with $\alpha = 4$ and $E_K \propto k^2$, we find $\beta = 1$, while in HD with $\alpha = 4$, we find $\beta = 3$. In agreement with earlier work [27], the following exceptions can

be identified: in HD with $1 \leq \alpha \leq 3$ and in nonhelical MHD with $1 \leq \alpha \leq$ we find $\beta = \alpha$ [20]. The only case where $\alpha = \beta = 4$ has been found is when the magnetic Prandtl number $\text{Pr}_M \equiv \nu/\eta$ is small; see Figs. 4(a) and (c) for $\text{Pr}_M = 0.01$. Here, the conservation of \mathcal{L} may actually apply [28]. For $\text{Pr}_M \equiv \nu/\eta \gg 1$, on the other hand, we find $\beta = 2$ scaling, even though $\alpha = 4$; see Figs. 4(d) and (f).

In conclusion, the present work has revealed robust properties of the scaling exponent β governing the time-dependence of the energy spectrum $E(k, t)$ through

$\xi^\beta \phi(k\xi)$ with a time-independent scaling function ϕ and a time-dependent integral scale $\xi(t)$. The helical case is particularly robust in that any point in the pq plane evolves along the $\beta = 0$ line ($p = q$) toward the point $p = q = 2/3$. Furthermore, if the initial spectrum has $\alpha = 2$, it first steepens to $\alpha = 4$ and then follows the same decay as with an initial $\alpha = 4$. Moreover, for a scale-invariant spectrum with $\alpha = -1$, we again find $\beta = 0$, i.e., the same as for $\alpha = 2$ and 4, but now with $p_M \approx q_M \approx 0.2$; see Fig. 3(f). In the fractionally helical case, points in the pq plane evolve toward the $\beta = 0$ line and, for $\alpha \geq 2$, later toward $p_M = q_M = 2/3$.

Our results have consequences for two types of cosmological initial magnetic fields: causal ones with $E_M \propto k^4$ will always be accompanied by a shallower kinetic energy spectrum $E_K \propto k^2$, thus favoring inverse transfer [23, 32], while a scale-invariant inflation-generated helical field exhibits self-similarity with $\beta = 0$ in the same way as for other initial slopes, but now with $p = q \approx 0.2$ instead of $2/3$. For decaying wind tunnel turbulence, Loitsiansky scaling is ruled out in favor of Saffman scaling, provided $\alpha = 2$. No inverse transfer is possible in HD, even if $\alpha = 4$, contrary to earlier claims [15]. The experimental realization of initial conditions with $\alpha \neq 2$ could be challenging for wind tunnels, but may well be possible in plasma experiments [33].

We thank Andrey Beresnyak, Leonardo Campanelli, Ruth Durrer, Alexander Tevzadze, and Tanmay Vachaspati for useful discussions. Support through the NSF Astrophysics and Astronomy Grant Program (grants 1615940 & 1615100), the Research Council of Norway (FRINATEK grant 231444), the Swiss NSF SCOPES (grant IZ7370-152581), and the Georgian Shota Rustaveli NSF (grant FR/264/6-350/14) are gratefully acknowledged. We acknowledge the allocation of computing resources provided by the Swedish National Allocations Committee at the Center for Parallel Computers at the Royal Institute of Technology in Stockholm. This work utilized the Janus supercomputer, which is supported by the National Science Foundation (award number CNS-0821794), the University of Colorado Boulder, the University of Colorado Denver, and the National Center for Atmospheric Research. The Janus supercomputer is operated by the University of Colorado Boulder.

- [5] I. P. Castro, *J. Fluid Mech.* **93**, 631 (1979).
- [6] D. K. Lilly, *J. Atmos. Sci.* **40**, 749 (1983).
- [7] M.-M. Mac Low, R. S. Klessen, and A. Burkert, *Phys. Rev. Lett.* **80**, 2754 (1998).
- [8] K. Subramanian, A. Shukurov, and N. E. L. Haugen, *Mon. Not. R. Astron. Soc.* **366**, 1437 (2006).
- [9] M. Christensson, M. Hindmarsh, and A. Brandenburg, *Phys. Rev. E* **64**, 056405 (2001).
- [10] R. Banerjee, K. Jedamzik, *Phys. Rev. D* **70**, 123003 (2004).
- [11] A. Brandenburg, K. Enqvist, and P. Olesen, *Phys. Rev. D* **54**, 1291 (1996).
- [12] L. Campanelli, *Eur. Phys. J. C* **76**, 504 (2016).
- [13] Wagstaff, J. M. and R. Banerjee, *J. Cosmol. Astropart. Phys.* **01** (2016) 002.
- [14] W. K. George, *Phys. Fluids* **4**, 1492 (1992).
- [15] P. Olesen, *Phys. Lett. B* **398**, 321 (1997).
- [16] C. Kalelkar and R. Pandit, *Phys. Rev. E* **69**, 046304 (2004).
- [17] Campanelli, L., *Phys. Rev. D* **70**, 083009 (2004).
- [18] A. G. Tevzadze, L. Kisslinger, A. Brandenburg, T. Kahniashvili, *Astrophys. J.* **759**, 54 (2012).
- [19] <https://github.com/pencil-code>
- [20] See Supplemental Material for tests regarding the accuracy of the scheme and the assumption of isothermality and other properties of decaying MHD turbulence in arXiv:1607.01360, which includes Refs. [21, 22].
- [21] A. Brandenburg and W. Dobler, *Comp. Phys. Comm.* **147**, 471 (2002).
- [22] A. Brandenburg, (ed. A. Ferriz-Mas & M. Núñez), pp. 269. *Advances in nonlinear dynamos (The Fluid Mechanics of Astrophysics and Geophysics, Vol. 9)* (2003). Taylor & Francis, London and New York
- [23] A. Brandenburg, T. Kahniashvili, and A. G. Tevzadze, *Phys. Rev. Lett.* **114**, 075001 (2015).
- [24] J. Zrake, *Astrophys. J.* **794**, L26 (2014).
- [25] P. Olesen, arXiv:1509.08962 (2015).
- [26] H. S. Kang, S. Chester, and C. Meneveau, *J. Fluid Mech.* **480**, 129 (2003).
- [27] Yousef, T. A., Haugen, N. E. L., & Brandenburg, A., *Phys. Rev. E* **69**, 056303 (2004).
- [28] P. A. Davidson, *J. Fluid Mech.* **663**, 268 (2010).
- [29] P. G. Saffman, *Phys. Fluids* **10**, 1349 (1967).
- [30] N. E. L. Haugen and A. Brandenburg, *Phys. Rev. E* **70**, 026405 (2004).
- [31] P. Olesen, arXiv:1511.05007 (2015).
- [32] T. Kahniashvili, A. G. Tevzadze, A. Brandenburg, and A. Neronov, *Phys. Rev. D* **87**, 083007 (2013).
- [33] C. B. Forest, K. Flanagan, M. Brookhart, et al., *J. Plasma Phys.* **81**, 345810501 (2015).

-
- [1] G. K. Batchelor and I. Proudman, *Phil. Trans. Roy. Soc. Lond. A*, **248**, 369 (1956).
 - [2] A. Pouquet, U. Frisch, and J. Léorat, *J. Fluid Mech.* **77**, 321 (1976).
 - [3] D. Biskamp and W.-C. Müller, *Phys. Rev. Lett.* **83**, 2195 (1999).
 - [4] S. R. Stalp, L. Skrbek, and R. J. Donnelly, *Phys. Rev. Lett.* **82**, 4831 (1999).

Supplemental Material

to “Classes of hydrodynamic and magnetohydrodynamic turbulent decay” (arXiv:1607.01360)

by A. Brandenburg & T. Kahniashvili

EFFECT OF PHASE ERRORS

By default, the PENCIL CODE uses sixth order accurate finite difference representations for the first and second derivatives. A low spatial order of the scheme implies that at high wavenumbers the magnitude of the numerical derivative is reduced, leading to lower advection speeds of the high wavenumber Fourier components. This is generally referred to as phase error. Thus, for an advected tophat function, the high wavenumber constituents will lag behind, creating the well-known Gibbs phenomenon which needs to be controlled by a certain amount of viscosity. Higher order schemes require less viscosity to control the Gibbs phenomenon [21]. On the other hand, any turbulence simulation requires a sufficient amount of viscosity to dissipate kinetic energy. It is therefore thought that for a sixth orders scheme the two limits on the viscosity are similar and that it is not advantageous to use higher order representations of the spatial derivatives.

To verify this in the present context, we have run a high Reynolds number case both with sixth and tenth order schemes. In the PENCIL CODE, the order of the scheme can easily be changed by setting `DERIV=deriv_10th`. In that case, first and second derivatives are represented as

$$d^n f_i / dx^n = \sum_{j=-N}^N (\text{sgn} j)^n c_{|j|}^{(n)} f_{i+j} / \delta x^n, \quad (7)$$

with coefficient $c_j^{(n)}$ given in Table II for schemes of order N . The result of the comparison is shown in Fig. 5.

TABLE II: Coefficients $c_j^{(n)} \equiv a_j^{(n)} / b^{(n)}$

N	n	$b^{(n)}$	$a_0^{(n)}$	$a_1^{(n)}$	$a_2^{(n)}$	$a_3^{(n)}$	$a_4^{(n)}$	$a_5^{(n)}$
10	1	2520	0	2100	-600	150	-25	2
8	1	840	0	672	-168	32	-3	
6	1	60	0	45	-9	1		
4	1	12	0	8	-1			
2	1	2	0	1				
10	2	25200	-73766	42000	-6000	1000	-125	8
8	2	5040	-14350	8064	-1008	128	-9	
6	2	180	-490	270	-27	2		
4	2	12	-30	16	-1			
2	2	1	-2	1				

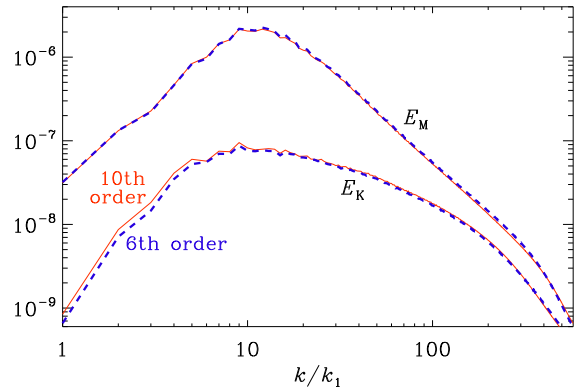


FIG. 5: Magnetic (upper curves) and kinetic (lower curves) energy spectra for at $t = 110$ for the sixth order (blue, dashed) and tenth order (red, solid) finite difference schemes.

The differences between the two cases are negligible, except that with the more accurate tenth order scheme the inverse transfer of kinetic energy to larger scales is now slightly stronger. This is consistent with our earlier findings that the inverse transfer in nonhelical MHD becomes more pronounced at larger resolution.

ISOTHERMAL VERSUS POLYTROPIC EQUATION OF STATE

An isothermal equation of state is often used in subsonic compressible turbulence to approximate the conditions of nearly incompressible flows. Using instead a polytropic equation of state means that in the momentum equation the pressure gradient term for an isothermal gas is amended by a factor $\propto \rho^{\gamma-1}$, i.e.,

$$c_s^2 \nabla \ln \rho \rightarrow c_{s0}^2 \left(\frac{\rho}{\rho_0} \right)^{\gamma-1} \nabla \ln \rho, \quad (8)$$

where $\gamma = 5/3$ is the polytropic index for a monatomic gas instead of $\gamma \rightarrow 1$ for an isothermal gas. Using $\gamma = 5/3$ implies a slightly stiffer equation of state, so one has to drive stronger to achieve the same compression; see Sect. 9.3.6 of [22]. In the present context of subsonic decaying turbulence, this leads to slightly smaller vorticity fluctuations, as is shown in Fig. 6. It is seen that the difference between $\gamma = 5/3$ and 1 is negligible for all practical purposes.

TIME-DEPENDENT $\nu(t)$ AND $\eta(t)$

As pointed out by Olesen [15], the hydrodynamic and MHD equations are invariant under rescaling $x \rightarrow \tilde{x}\ell$ and $t \rightarrow \tilde{t}\ell^{1/q}$ provided also ν and η are being dynamically

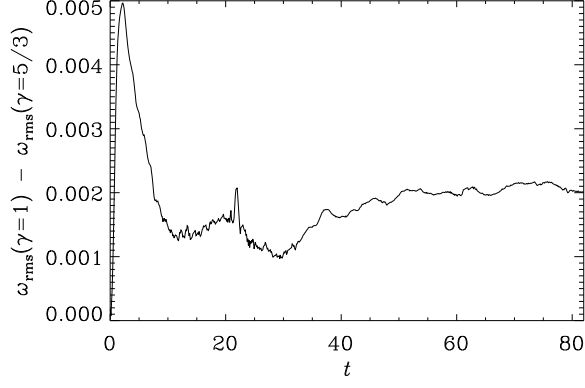


FIG. 6: Difference in rms vorticity, ω_{rms} , between the isothermal and polytropic solutions.

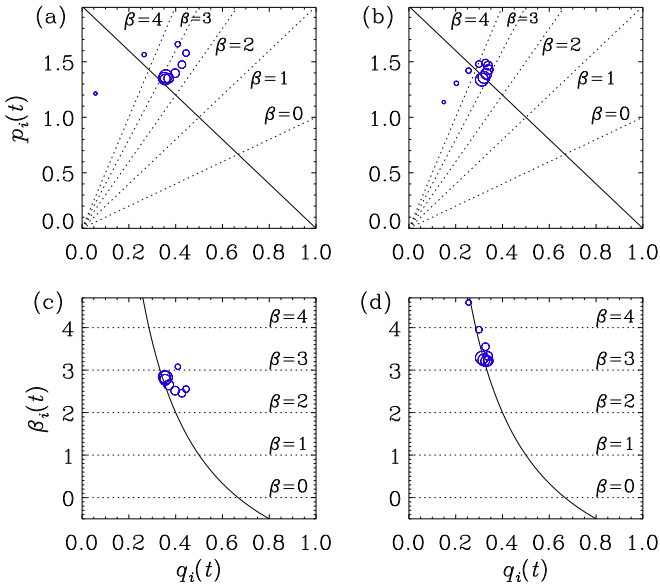


FIG. 7: pq diagrams for hydrodynamic turbulence with $\nu = \text{const}$ (a) and time-dependent $\nu(t) \propto t^r$ (b) with $r = -0.43$ and $\alpha = 4$. Panels (c) and (d) show the corresponding βq diagrams. Open (closed) symbols corresponds to $i = K$ (M) and their sizes increase with time.

rescaled such that

$$\nu(t) = \nu_0 \max(t/t_0, 1)^r, \quad \eta(t) = \eta_0 \max(t/t_0, 1)^r, \quad (9)$$

TABLE III: Exponents r for different α .

α	0	1	2	3	4
r	0.33	0	-0.20	-0.33	-0.43

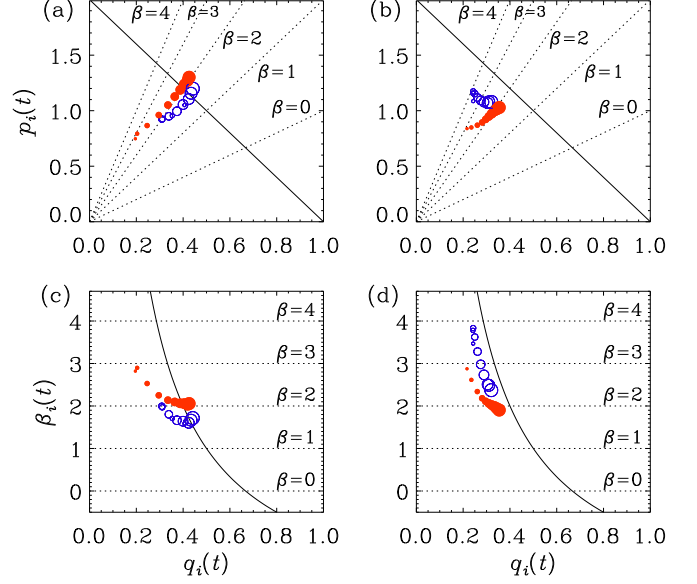


FIG. 8: Similar to Fig. 7, but for nonhelical MHD turbulence with $\nu = \eta = \text{const}$ (a) and time-dependent $\nu(t) = \eta(t) \propto t^r$ (b) with $r = -0.43$ and $\alpha = 4$.

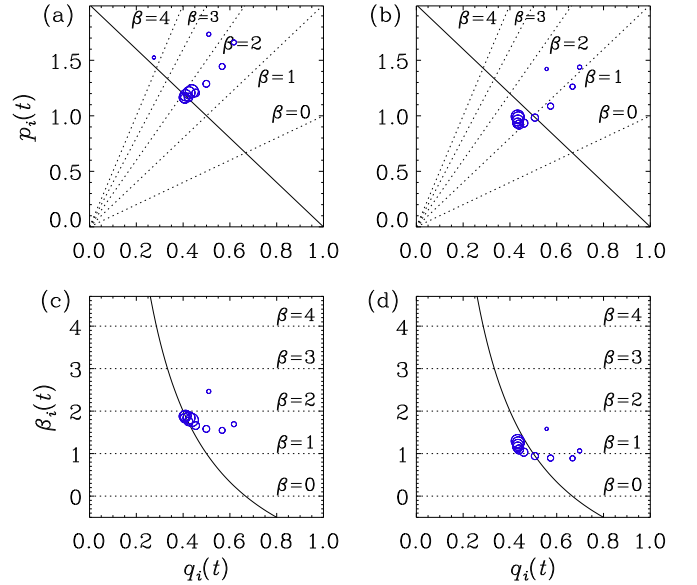


FIG. 9: Similar to Fig. 7, but for $\alpha = 2$ (a) and $\alpha = 1$ (b) with $\nu = \text{const}$.

with

$$r = 2q - 1 = (1 - \alpha)/(3 + \alpha); \quad (10)$$

see Table III. The use of the max function in Eq. (9) limits the values of $\nu \leq \nu_0$ and $\eta \leq \eta_0$ for $t \leq t_0$ when $r < 0$. At large Reynolds numbers, the time-dependence is not expected to be important. To verify this, we compare in Fig. 7 hydrodynamic runs with constant and time-dependent ν using $\alpha = 4$. Both cases are similar and the

case with time-dependent ν still has $\beta = 3 \neq \alpha$. Similar behavior is found in MHD; see Fig. 8, where we compare runs with constant and time-dependent ν and η using again $\alpha = 4$. In both cases, we find $\beta = 2 \neq \alpha$.

In agreement with earlier work we find that in hydrodynamic cases with $\alpha = 2$ and $\alpha = 1$, we have $\beta = \alpha$ [27]. This is demonstrated in Fig. 9, where we show the pq and βq diagrams for these two cases.